Experimental Analysis of Adiabatic Silicon Photonic Microring Resonators Under Process Variations

Asif Mirza, *Student Member, IEEE*, Ryan E. Gloekler, *Student Member, IEEE*, Joseph Thompson, *Student Member, IEEE*, Sudeep Pasricha, *Fellow, IEEE*, and Mahdi Nikdsast, *Senior Member, IEEE*

***Abstract*— This letter delves into the design and experimental analysis of adiabatic silicon photonic microring resonators (MRRs) under fabrication-process variations (FPVs). Compared to conventional MRRs, our experimental results captured by automatically characterizing over 550 fabricated devices highlight the superior performance of adiabatic MRRs to achieve better resonance-wavelength uniformity with 70% reduction on average in MRRs' resonance-wavelength shift. Additionally, adiabatic MRRs outperform conventional ones in other key metrics like uniformity in Quality (Q)-factor and extinction ratio. The adoption of adiabatic MRRs offers more robustness under FPVs and tuning-power savings, thus paving the way for more energy-efficient and scalable photonic integrated circuits (PICs).**

***Index Terms*— Silicon photonics, microring resonators, adiabatic rings, design optimization, design for manufacturability.**

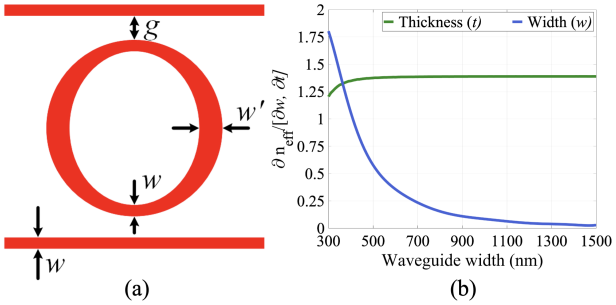

Fig. 1. (a) Adiabatic MRR with its design parameters ($w' > w$). (b) Rate of changes in the effective index (n_{eff}) w.r.t. the variations in the waveguide width (w) and thickness (t) as the waveguide width increases from 300 nm to 1500 nm (x axis).

I. Introduction

SILICON photonic microring resonators (MRRs) are circular waveguide structures used widely in photonic integrated circuits (PICs). They help realize efficient components such as optical filters, switches, and modulators while providing numerous advantages, including compact footprint (e.g., radius $\approx 3\mu$m) [1], high quality (Q)-factor [2], cost-effective fabrication on CMOS-compatible silicon substrates, low power consumption, and high speed operation [3]. Accordingly, MRRs have contributed to several integrated photonic applications in Datacom [4], and most recently in optical neural networks and neuromorphic computing [5].

There are, however, certain challenges to consider when employing MRRs in PICs. Temperature and fabrication-process variations (FPVs) impact device-to-device consistency (a.k.a. inter-device matching) [6] by imposing undesired resonance-wavelength shifts in MRRs. While active management and calibration techniques—such as incorporating sensors and feedback control systems with thermo-optic or electro-optic tuning [7]—can be employed to compensate for the inconsistencies in MRRs, such methods often lack scalability and lead to an increase in power consumption in PICs, which can easily exceed the power budget in a system consisting of tens of hundreds of MRRs. In addition to active compensation methods, MRRs can be designed to be more robust under variations. Prior work in [8], [9], [10], and [11] has shown that an adiabatic design of MRRs (see Fig. 1(a)) can help improve device robustness under variations. Such a design helps reduce phase errors and scattering losses, enabling higher transmission efficiency and overall improved performance, including better tolerance to FPVs.

Several prior works have investigated adiabatic MRRs. Luo et al. in [10] developed an MRR-based modulator with multi-mode waveguides to improve accuracy and repeatability of the MRRs' resonant wavelength. In their work, the ring waveguide width is increased to reduce phase errors associated with side-wall etching. Su et al. in [11] proposed the use of adiabatic rings to design MRRs with a high Q-factor of 27000 and improved tolerance to FPVs. The work in [12] presented an adiabatic MRR to enable terabit-per-second chip-to-chip optical I/O. The work in [13] proposed thermally tuned adiabatic MRRs with 0.49 nm/mW tuning efficiency and low resonance loss of 0.085 dB.

This letter presents a comprehensive experimental analysis of adiabatic MRRs to demonstrate their performance and robustness under FPVs. In addition, we discuss the design and analysis of adiabatic MRRs to facilitate their employment in PICs. Our experimental study includes the fabrication of

Manuscript received 7 September 2023; revised 20 December 2023; accepted 23 January 2024. Date of publication 29 January 2024; date of current version 21 February 2024. This work was supported by the National Science Foundation (NSF) under Grant CCF-1813370, Grant CCF-2006788, and Grant CNS-2046226. *(Corresponding author: Asif Mirza.)*

Asif Mirza, Joseph Thompson, Sudeep Pasricha, and Mahdi Nikdsast are with the Department of Electrical and Computer Engineering, Colorado State University, Fort Collins, CO 80523 USA (e-mail: asifmirz@colostate.edu; josephne@colostate.edu; sudeep@colostate.edu; mnikdast@colostate.edu).

Ryan E. Gloekler is with the Department of Electrical and Computer Engineering, University of California at Davis, Davis, CA 95616 USA (e-mail: regloekler@ucdavis.edu).

Color versions of one or more figures in this letter are available at https://doi.org/10.1109/LPT.2024.3359532.

Digital Object Identifier 10.1109/LPT.2024.3359532

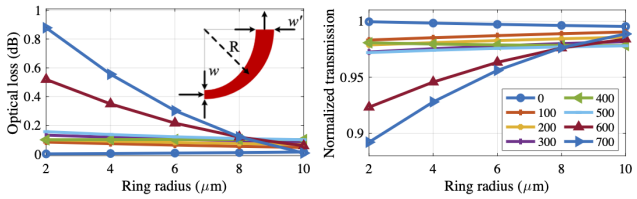

(a) Optical power loss (b) Transmission efficiency

Fig. 2. (a) Optical loss and (b) transmission efficiency in a tapered ring with different radii and input–output waveguide widths. Results are based on simulating the curved, tapered quarter ring (inset in (a)) with the radius of R and nonidentical input–output waveguide widths (w and w') using Lumerical FDTD. The legend shows the difference in waveguide width (i.e., $0\text{ nm} \leq |w' - w| \leq 700\text{ nm}$).

268 conventional (i.e., when $w = w'$ in Fig. 1(a)) and 289 adiabatic MRRs using electron-beam (E-Beam) lithography, and automatic characterization of all the MRRs to compare and study their tolerance to FPVs, and uniformity and performance in terms of Q-factor, extinction ratio, and free-spectral range. Characterization results show significant uniformity in the response of adiabatic MRRs and across all the performance metrics, compared to conventional MRRs.

The rest of the letter is organized as follows. Section II focuses on the design and analysis of adiabatic MRRs. Section III describes the experimental setup used, along with experimental analysis and comparisons of measurement results between conventional and adiabatic MRRs. Lastly, conclusions are presented in Section IV.

II. Adiabatic MRR Design and Analysis

Fig. 1(b) shows that with increasing the waveguide width, the rate of changes in the effective index (n_{eff}) w.r.t. the variations in the waveguide width (w) decreases, while such a rate remains almost the same under waveguide thickness (t) variations [8]. This implies that by increasing the waveguide width in an MRR, one should expect higher tolerance under FPVs in the device. However, uniformly increasing the waveguide width (i.e., increasing $w = w'$ in Fig. 1(a) together) in an MRR will result in undesired optical mode distortion and excitation, as indicated in our prior work [8]. This necessitates an adiabatic MRR design using curved, tapered waveguides within the ring (as further discussed later in this section) by gradually increasing the ring waveguide's width from the input (i.e., w) to the center (i.e., w'), as shown in Fig. 1(a), to avoid optical mode distortions and excitation of higher order modes in the MRR. Note that in an adiabatic MRR design, the coupling region between the input/drop waveguide and the ring is the same as that in a conventional MRR, all following the same waveguide width (i.e., w, where $w < w'$).

The resonant wavelength (λ_R^a) in an adiabatic MRR can be modeled based on its effective index (n_{eff}^a) as:

$$\lambda_R^a = \left(\frac{2\pi R}{m}\right) n_{eff}^a, \tag{1}$$

where R is the radius of the MRR and m is an integer that denotes the order of the resonance. Also, n_{eff}^a can be approximated by taking the average of effective indices when considering w and w' waveguide widths: i.e., $n_{eff}^a = \frac{1}{2}\left(n_{eff}(w) + n_{eff}(w')\right)$. Accordingly, λ_R^a in an adiabatic MRR is impacted by the critical dimensions of the MRR and its radius, slight variations (e.g., due to FPVs) in which will deviate λ_R^a, which is known as the resonance-wavelength shift ($\delta\lambda_R^a$). In order to model $\delta\lambda_R^a$ in an adiabatic MRR, a compact model can be defined based on:

$$\delta\lambda_R^a = \left(\frac{\lambda_R^a |n_{eff}^a - n_{eff}^{a\dagger}|}{n_g^a}\right) + \left(\frac{\lambda_R^a R^\dagger}{R}\right)\frac{n_{eff}^a}{n_g^a}, \tag{2}$$

where $n_{eff}^{a\dagger}$ and $R^\dagger$ are the effective index and radius of the MRR that have changed due to FPVs, and n_g^a is the ideal group index in the MRR, which can be calculated using n_{eff}^a. According to (2) and Fig. 1(b), compared to conventional MRRs, adiabatic MRRs should benefit from reduced $\delta\lambda_R^a$ by carefully designing w and w' (see Section III).

To realize a robust, adiabatic MRR, one needs to use curved, tapered waveguides within the ring structure (see Fig. 1(a)). We simulated different curved, tapered waveguides using Lumerical finite-difference time-domain (FDTD) simulation [14] to analyze fundamental TE-mode transmission efficiency when light traverses a tapered ring with nonidentical input (w) and output (w') waveguide widths (see the inset in Fig. 2(a)). Fig. 2(a) shows the optical losses in this structure accounting for the bending loss, propagation loss, and mode-mismatch loss due to using different waveguide widths under different ring radii (see the x-axis). The transmission efficiency is shown in Fig. 2(b) in which transmission at $|w' - w| = 0$ accounts for losses in a conventional ring. As can be seen in Fig. 2, larger radii is required when $|w' - w|$ increases to compensate for inefficiencies in the ring and improve transmission efficiency in the tapered ring structure.

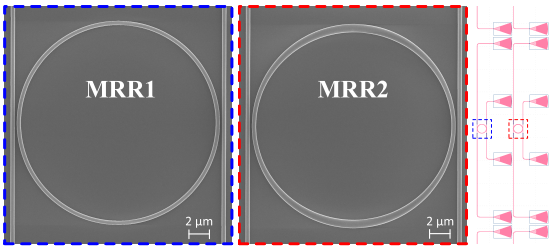

(a) (b) (c)

Fig. 3. Scanning electron microscopic (SEM) images of fabricated (a) conventional and (b) adiabatic MRRs taken from part of the chip. (c) The unit cell of the fabricated MRRs.

TABLE I
MRR Test Structure Design Parameters (See Fig. 1)

	Radius (R)	Gap (g)	Width (w)	Width (w')
MRR1	9.935 μm	100 nm	450 nm	450 nm
MRR2	9.935 μm	100 nm	450 nm	820 nm

III. Experimental Results and Discussion

By utilizing the MRR design-space exploration framework developed in our prior work [8]—to which we added resonance-wavelength shift model in adiabatic MRRs (i.e., (2)) and results from Fig. 2—we designed two TE-polarized MRR test structures namely MRR1 (conventional MRR) and MRR2 (adiabatic MRR), based on add-drop structures, as shown in Fig. 3. The design parameters of each MRR are listed in Table I, optimized in a way to design MRR1 and MRR2 with the same overall size so that they experience similar FPVs while keeping their nominal resonant wavelengths as close as possible (i.e., 1550 nm in MRR1 and 1546 nm in MRR2). Note that the resonant wavelength difference between MRR1

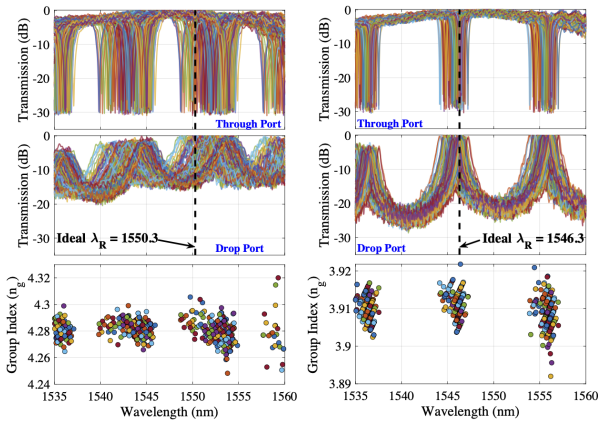

(a) Conventional MRR (MRR1) (b) Adiabatic MRR (MRR2)

Fig. 4. Through-port and drop-port response in (a) conventional and (b) adiabatic MRRs. Bottom figures show the resonant wavelength versus corresponding group index (n_g) to find responses that belong to the same resonant mode. Black-dotted lines show the ideal (nominal) resonant wavelengths.

and MRR2 does not hinder our analysis in this letter. Moreover, 268 identical copies of MRR1 and 289 identical copies of MRR2 were strategically placed across a 10 × 10 mm chip fabricated using a standard E-Beam multi-project wafer (MPW) process at Applied Nanotools Inc. [15], where each pair of MRR1 and MRR2 were placed as close as possible (see Fig. 3(c)) to ensure that they experience similar FPVs.

We tested the chip using an automated testing station from Maple Leaf Photonics that has a capability to test a single die as large as 25 × 25 mm. In addition to the testing station, the test setup consists mainly of four parts: a laser source, a polarization controller set to TE, a fiber array attached to the station, and a photodetector. The chip stage was fixed and the fiber arm provided automatic movement in the X, Y, Z, yaw, and pitch directions. These movements are critical for efficient alignment of the fiber array with the chip to perform low-loss measurements. Coupling to the GCs on the chip was achieved using a single-mode fiber array with a 127 μm pitch. For precise alignment of the chip with the fiber array, we utilized two digital microscopic cameras integrated into our testing station. The laser source, produced by Agilent HP 8164A, operates within the C-band, spanning a wavelength range of 1460 nm to 1580 nm and offering a resolution of 0.1 pm. Light detection from the chip was performed with the Keysight 81635A dual optical photodetector, which covers a wavelength range from 800 nm to 1650 nm with a power spectrum from +10 to −80 dBm. All connections within the setup were established using single-mode fibers. Moreover, the temperature of the chip stage was maintained at 300 K to eliminate the impact of thermal variations during the measurements. The input power was set to 7.5 dBm, for which we experienced a total loss of 25.2 dB in the output. The loss due to grating couplers was 17.6 dB (i.e., 8.8 dB each), and the loss for each device was estimated to be ≈1 dB (see Table II). Accordingly, the total unaccounted losses due to the test and alignment was ≈6.6 dB.

We begin by comparing the total resonance-wavelength shift between the conventional and adiabatic MRRs. Note that it is crucial to observe the same resonant mode when analyzing the resonant shift, given the fact that the resonance-wavelength

TABLE II

CHARACTERIZED DEVICE PERFORMANCE (AVG.: AVERAGE, SD: STANDARD DEVIATION, λ_R: RESONANT WAVELENGTH, ER: EXTINCTION RATIO)

	MRR1 (Conventional)		MRR2 (Adiabatic)	
	Through	**Drop**	**Through**	**Drop**
Avg. λ_R	1552.8 nm		1546.1 nm	
SD λ_R ($\propto \delta\lambda_R$)	1.3 nm		0.5 nm	
Avg. Q-factor	3567	590	10067	790
Avg. ER	27.7 dB	12.8 dB	25 dB	21.8 dB
Crosstalk	−22.6 dB	−12.3 dB	−21.2 dB	−19.6 dB
Drop loss	1.3 dB		0.8 dB	

shift may exceed the free-spectral range (FSR) in an MRR. To verify we are examining the correct resonant mode, we compute the group index (n_g) for every resonant wavelength by using $FSR = \frac{\lambda_R^2}{n_g \cdot L}$, in which λ_R denotes the resonant wavelength and L is the MRR's round trip length. Note that FSR can be directly estimated from measured through-/drop-port response. Based on this method, initially proposed in [16], the MRR responses belonging to the same resonant mode will have close group indices, hence can be identified by observing the resonant wavelength versus group index plot.

Figs. 4(a) and 4(b) show the measured through- and drop-port responses for the conventional (MRR1) and adiabatic (MRR2) MRRs, respectively. For each captured resonant wavelength, we also calculated the corresponding group index, the result for which is shown in the bottom plots in Fig. 4 where clusters of data points show resonant wavelengths that correspond to the same resonant mode. Considering this analysis, our observation is that the resonance-wavelength shift measured does not surpass the FSR in any MRR.

Considering the through- and drop-port responses in Fig. 4, the adiabatic MRRs' responses align closer to the *ideal response* at 1546.3 nm by up to 70% on average, compared to the conventional MRRs whose *ideal response* is at 1550.3 nm. For a more complete experimental comparison between MRR1 and MRR2, Table II shows our measurement results across multiple performance metrics. The average responses for each MRR (close to 1550 nm resonant mode) calculated considering all the responses captured are 1552.8 nm and 1546.1 nm for MRR1 and MRR2, respectively, while the corresponding standard deviations (proportional to the measured resonance-wavelength shifts—$\delta\lambda_R$) for MRR1 and MRR2 are, respectively, 1.3 nm and 0.5 nm, showing significant uniformity in the responses of adiabatic MRRs compared to the conventional ones (see Avg. λ_R and SD λ_R in Table II). Table II also compares experimentally measured Q-factor, extinction ratio (ER), crosstalk, and drop loss between MRR1 and MRR2. The drop loss in each device is estimated based on the Q-factor and attenuation-factor analysis in each MRR. Also, the crosstalk was measured based on the minimum and maximum transmissions observed at the through and drop ports. As can be seen, our experimental results show that the adiabatic design results in a better performance in general.

To further analyze the resonance-wavelength shift across all the devices on the chip, we compared the resonance-wavelength difference ($\Delta\lambda_R$) between each pair of MRRs—of the same type: either conventional or adiabatic—positioned at different locations on the chip. The result of

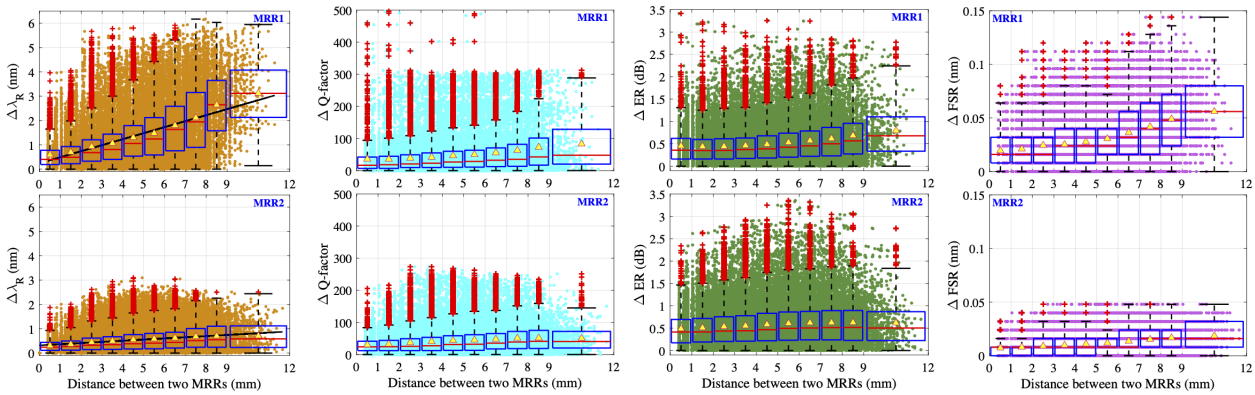

(a) Resonance-wavelength difference (b) Q-factor difference (c) Extinction ratio (ER) difference (d) FSR difference

Fig. 5. Comparison of various performance metrics represented with different colors between each pair of MRRs placed at different positions on the chip (x axis). Yellow triangles show the average within each box, to which a linear fit (shown as black line) is depicted in (a). For each box, the red plus signs represent the outliers that fall outside the typical range and the red lines show the median within each box.

this analysis in shown in Fig. 5(a). As can be seen, both conventional and adiabatic MRRs positioned in proximity exhibit more similar responses (i.e., smaller $\Delta\lambda_R$) compared to those spaced farther apart. In addition, $\Delta\lambda_R$ escalates as the distance between the MRRs increases. This observation confirms a strong linear correlation (see the black lines—fit to the average in each boxplot—in Fig. 5(a)) between MRR placement and resonance uniformity, as showed also by [16]. Another important observation from Fig. 5(a) is that, with increasing distance between each pair of MRR (x-axis in the figure), the average $\Delta\lambda_R$ in MRR2 (adiabatic) is much smaller than that in MRR1 (conventional), exhibiting 50% reduction in $\Delta\lambda_R$ on average. More importantly, the resonance-wavelength difference among adiabatic MRRs across the entire chip, even when two of them are placed as far as >9 mm, stays within <1 nm.

We also analyzed the difference in Q-factor, ER, and FSR for each pair of MRRs placed at different locations on the chip, results of which are shown in Figs. 5(b), 5(c), and 5(d), respectively. The Q-factor was estimated by performing a Lorentzian fit to the captured responses and analyzing the full-width half-maximum (FWHM), and correspondingly the Q-factor. Compared to the conventional MRRs, we observe that for all Q-factor, ER, and FSR, the adiabatic MRRs' performance is more uniform and almost independent of the MRRs' placement, when considering each MRR pair and their placement distance (x-axis in the figures).

IV. Conclusion

In this letter, we described our experimental analysis that compares fabricated conventional and adiabatic MRR designs. Our findings consistently demonstrate the superior attributes of adiabatic MRRs over their conventional counterparts. Notably, adiabatic MRRs exhibit a remarkable 70% alignment with ideal resonant wavelengths for which they are designed. Moreover, compared to conventional MRRs, adiabatic MRRs show significant uniformity in terms of frequency response, Q-factor, extinction ratio, and FSR. Such significant uniformity in adiabatic MRRs make them promising designs for many PIC applications, both in Datacom and computation, where high inter-device matching is required. Furthermore, the high uniformity helps simplify device placement and routing, as well as tuning by allowing for collectively tuning all of MRRs (as compared to individual tuning), hence reducing tuning complexity and overall power overhead.

References

[1] D. Shekhawat and R. Mehra, "Design of ultra-compact and highly-sensitive graphene assisted silicon micro-ring resonator modulator for switching applications," *Silicon*, vol. 14, no. 8, pp. 4383–4390, Jun. 2022.

[2] X. Zhang et al., "High Q-factor, ultrasensitivity slot microring resonator sensor based on chalcogenide glasses," *Opt. Exp.*, vol. 30, no. 3, p. 3866, Jan. 2022.

[3] Y. Yuan et al., "A 100 Gb/s PAM4 two-segment silicon microring resonator modulator using a standard foundry process," *ACS Photon.*, vol. 9, no. 4, pp. 1165–1171, Apr. 2022.

[4] L. He et al., "Broadband athermal waveguides and resonators for datacom and telecom applications," *Photon. Res.*, vol. 6, no. 11, p. 987, 2018.

[5] B. J. Shastri et al., "Photonics for artificial intelligence and neuromorphic computing," *Nature Photon.*, vol. 15, no. 2, pp. 102–114, Feb. 2021.

[6] C. Sun et al., "A 45nm SOI monolithic photonics chip-to-chip link with bit-statistics-based resonant microring thermal tuning," in *Proc. Symp. VLSI Circuits (VLSI Circuits)*, Jun. 2015, pp. C122–C123.

[7] P. Pintus, "PWM-driven thermally tunable silicon microring resonators: Design, fabrication, and characterization," *Laser Photon. Rev.*, vol. 13, no. 9, 2019, Art. no. 1800275.

[8] A. Mirza, F. Sunny, P. Walsh, K. Hassan, S. Pasricha, and M. Nikdast, "Silicon photonic microring resonators: A comprehensive design-space exploration and optimization under fabrication-process variations," *IEEE Trans. Comput.-Aided Design Integr. Circuits Syst.*, vol. 41, no. 10, pp. 3359–3372, Oct. 2022.

[9] J. C. Mikkelsen, W. D. Sacher, and J. K. S. Poon, "Adiabatically widened silicon microrings for improved variation tolerance," *Opt. Exp.*, vol. 22, no. 8, p. 9659, 2014.

[10] Y. Luo et al., "A process-tolerant ring modulator based on multi-mode waveguides," *IEEE Photon. Technol. Lett.*, vol. 28, no. 13, pp. 1391–1394, Apr. 8, 2016.

[11] Z. Su et al., "Reduced wafer-scale frequency variation in adiabatic microring resonators," in *Proc. OFC*, Mar. 2014, pp. 1–3.

[12] D. Kramnik et al., "Fast-tuning adiabatic microrings for CROW filters and athermal WDM receivers in a 45 nm SOI CMOS process," in *Proc. CLEO, Sci. Innov.*, May 2022, p. SF4M-2.

[13] A. S. Khope. (2021). *Ultralow Loss Adiabatic Microring Resonator With Thermal Tuning*. [Online]. Available: https://doi.org/10.20944/preprints202106.0186.v1

[14] Ansys Lumerical. Accessed: 2024. [Online]. Available: https://www.lumerical.com/products/

[15] Appl. Nanotools Inc. Accessed: 2024. [Online]. Available: https://www.appliednt.com

[16] L. Chrostowski, X. Wang, J. Flueckiger, Y. Wu, Y. Wang, and S. T. Fard, "Impact of fabrication non-uniformity on chip-scale silicon photonic integrated circuits," in *Proc. OFC*, Mar. 2014, pp. 1–3.